Information Fusion 11 (2010) 114–123

Contents lists available at ScienceDirect

Information Fusion

journal homepage: www.elsevier.com/locate/inffus

MRI and PET image fusion by combining IHS and retina-inspired models

Sabalan Daneshvar [1], Hassan Ghassemian *

Department of Electrical and Computer Engineering, Tarbiat Modares University, Tehran, Iran

ARTICLE INFO

Article history:
Received 14 June 2007
Received in revised form 6 October 2008
Accepted 13 May 2009
Available online 20 May 2009

Keywords:
Image fusion
IHS (intensity-hue-saturation)
Retina-inspired model (RIM)
MRI (magnetic resonance imaging)
PET (positron emission tomography)

ABSTRACT

Image fusion has become a widely used tool for increasing the interpretation quality of images in medical applications. The acquired data might exhibit either good functional characteristic (such as PET) or high spatial resolution (such as MRI). The MRI image shows the brain tissue anatomy and contains no functional information. The PET image indicates the brain function and has a low spatial resolution. Hence, the image fusion task is carried out to enhance the spatial resolution of the functional images by combining them with a high-resolution anatomic image. A perfect fusion process preserves the original functional characteristics and adds spatial characteristics to the image with no spatial distortion. The intensity-hue-saturation (IHS) algorithm and the retina-inspired model (RIM) fusion technique can preserve more spatial feature and more functional information content, respectively. The presented algorithm integrates the advantages of both IHS and RIM fusion methods to improve the functional and spatial information content. Visual and statistical analyses show that the proposed algorithm significantly improves the fusion quality in terms of: entropy, mutual information, discrepancy, and average gradient; compared to fusion methods including, IHS, Brovey, discrete wavelet transform (DWT), à-trous wavelet and RIM.

1. Introduction

Medical imaging is divided into structural and functional systems. MRI and CT (computed tomography) provide high-resolution images with structural and anatomical information. PET (positron emission tomography) and SPECT (single-photon emission computed tomography) images provide functional information with low spatial resolution. In recent years, the success of PET-MRI imaging in the clinical field has triggered considerable interest in noninvasive functional and anatomical imaging. The limited spatial resolution in PET images has often resulted unsatisfactory in morphological analysis. Combining anatomical and functional tomographic datasets provide much more qualitative detection and quantitative determination in this area [1–5]. In this paper, we assume PET images are shown in pseudo-color, and therefore, treat them as color images.

Image fusion is the process of integrating information from two or more images of an object into a single image that is more informative and appropriate for visual perception or computer analysis. The purpose of image fusion is to decrease ambiguity and minimize redundancy in the output while maximizing the relative information specific to an application [6].

Prospective algorithms for the fusion are generally classified into three categories:

(1) Substitution methods, such as IHS and PCA (Principal Component Analysis) fusion methods [7,8].
(2) Arithmetic combination, such as Brovey, SVR (Synthetic Variable Ratio) and RE (Ratio Enhancement) [9].
(3) Multi-resolution fusion methods, which introduce spatial features from the high-resolution images into the multispectral (color) images, such as RIM, wavelets, Gaussian Laplacian pyramid techniques [10–15].

The multi-resolution fusion techniques have been discussed widely in the recent studies because of their advantages over the other fusion techniques. The IHS technique has been most commonly used in the practical applications [7,16], but, this technique can lead to spectral distortion in the results [17]. It is desirable that the fusion process preserves the original color information of PET image and the spatial characteristics of MRI image as much as possible [16], in the sense that only the complementary spatial information existing in MRI data be introduced into the PET.

To avoid the weak points of the IHS fusion technique and those of the retina-inspired technique, an IHS and RIM integrated fusion approach has been proposed in this study. The results show that the proposed algorithm significantly improves the fusion quality in terms of entropy, mutual information, discrepancy, and average gradient compared to other fusion methods.

This paper builds on the research formerly presented in [10] and its main contributions are as follows:

* Corresponding author. Tel.: +98 21 44213588; fax: +98 21 82884325.
E-mail address: ghassemi@modares.ac.ir (H. Ghassemian).
[1] Present address: Department of Electrical and Computer Engineering, Sahand University of Technology, Tabriz, Iran.

1566-2535/$ - see front matter © 2009 Elsevier B.V. All rights reserved.
doi:10.1016/j.inffus.2009.05.003

- Presenting a comprehensive theoretical basis behind the design of our algorithm.
- Describing the RIM fusion method.
- Explaining the IHS fusion method and its ability and deficiency.
- Proposing the use of a model based on integrated IHS and RIM to improve the fusion performance.
- Using three databases for performance evaluation, compared to IHS cylinder model, IHS triangular model, Brovey, DWT, à-trous wavelet and RIM methods. These methods are commonly used to evaluate the new methods [6–10].
- Analyzing the proposed method statistically by mutual information (entropy), discrepancy, and average gradient criteria.

Sections 2 and 3 discuss the RIM and IHS methods, respectively. In Section 4, we present the proposed integrated model. The experimental results and discussions are described in Section 5. Concluding remarks are discussed in Section 6.

2. Retina-inspired model (RIM)

Fig. 1 depicts retinal layers and major cell types inspired by the retinal model in [18,19] The photonic visual perception begins with the scene captured by cone and rod photoreceptors. The cones are highly sensitive to color, and the rods are sensitive to low light intensity, which is not required for the current research, however, the cones are significant. Image luminance is transmitted by the cone layer to the downstream retina and cortical layers. From the cone to ganglion layers, a pipeline of cellular layers can be identified. A pipeline can be classified into two functionality categories: the outer plexiform layer (OPL) and the inner plexiform layer (IPL), [18,19].

OPL properties are generated by the synaptic triad, which is composed of interconnected cells [20]:

– The cone cells form a transduction and regularization processing. The transduction converts luminance into electrochemical potentials at the downstream layers. The regularization process consists of a low-pass filtering. The cone cells are defined in terms of their functions (spectral sensibilities: red, green, and blue colors). Furthermore, their behaviors are locally depended on the luminance intensity and contrast;

$$cone[\vec{r}] = I[\vec{r}] * G(\vec{r}; \sigma_{cone}) - k_{horz}.horz[\vec{r}] \quad (1)$$

where $\vec{r}$ is a two-dimensional spatial position vector, $I[\vec{r}]$ indicates the input image stimulus intensity, $G(\vec{r}; \sigma_{cone})$ is a Gaussian operator and σ_{cone} is the cone cell Gaussian width, k_{horz} (set to 0.8) shows the horizontal cell signal weight and $horz[\vec{r}]$ is the horizontal cell output.

– The horizontal cells form a layer of strong regularization processing. The output response is performed by the cones output to elaborate a spatial average of the image intensity [20];

$$horz[\vec{r}] = cone[\vec{r}] * G(\vec{r}; \sigma_{horz}) \quad (2)$$

where $cone[\vec{r}]$ is the cone cell output, and σ_{horze} is the horizontal cell Gaussian width.

– The bipolar cells create the difference between the horizontal cell and the cone outputs. Bipolar cells are classified according to their shapes, their types of response and their functions.

The bipolar axons transmit the OPL outputs to the IPL area. The IPL processing is carried out by ganglion cells.

$$BP[\vec{r}] = cone[\vec{r}] - horz[\vec{r}] \quad (3)$$

where $BP[\vec{r}]$ is the bipolar cell output [20]

– The ganglion cells have a receptive field organized like concentric circles. The ganglion cells are also classified based on their shapes, their types of response and their functions. The effect of amacrine cells is ignored in our inspired model:

$$Gang[\vec{r}] = BP[\vec{r}] \quad (4)$$

If the retina plainly transmits the opposite-contrast directly from the photoreceptors to the brain, the resulting vision would be coarse-grained and blurry. Further processing in the retina describes precise edges and lets us focus on fine and minute details. The image sharpening and clearing starts at the first synaptic level in the retina, where the horizontal cells receive the cones output.

In a simplified model, the retina can be seen as performing a discrete convolution of the input image with a retinal filter kernel. In other words, it could be modeled by a discrete, linear filter. Each output of a ganglion cell represents the filter output at a particular position, coded in a spike train. The retinal filter kernels have a center-surround organization, where its general model is a Difference of-Gaussian (DoG). It consists of two Gaussians with different variances and in general can be written as [10,21,22]:

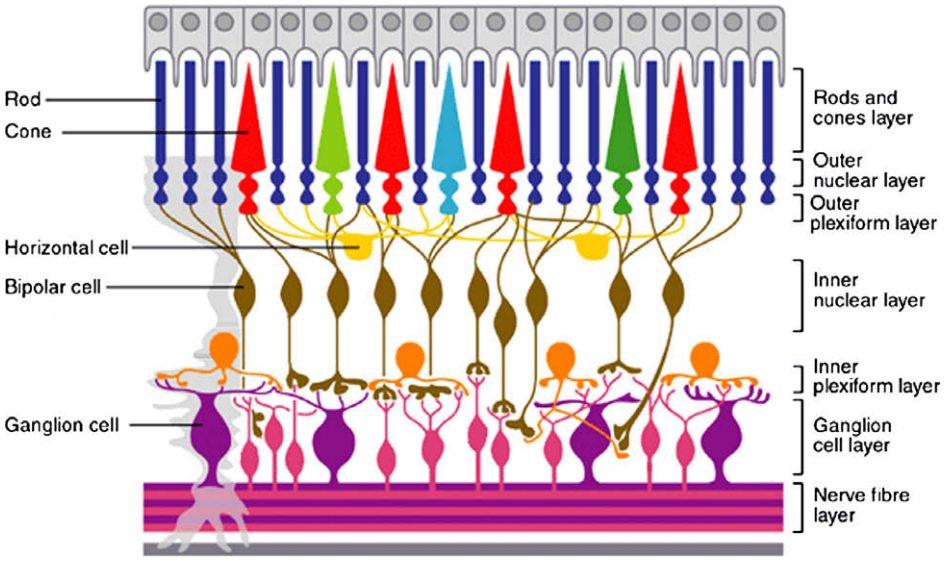

Fig. 1. The retinal layers and major groups of cell types [18,19].

$$CS(\vec{r}) = \alpha_c G(\vec{r};\sigma_c) - \alpha_s G(\vec{r};\sigma_s), \tag{5}$$

$$G(\vec{r};\sigma) = \frac{1}{2\pi\sigma^2}\exp\frac{-|\vec{r}|^2}{2\sigma^2}, \tag{6}$$

where α_c and α_s are weights of center and surround inputs (both set to 1.0). Both G_{σ_c} and G_{σ_s} are spatially lowpass filters. This depicts the filtering process which is taking place by the cone receptors (G_{σ_c}, the center signal) and by the horizontal cells (G_{σ_s}, the surround signal), respectively. The bandwidth of lowpass filter G_{σ_s} is less than G_{σ_c}, meaning $\sigma_s > \sigma_c$ (in this paper $\sigma_s = 2\sigma_c$). It corresponds to the biological fact that horizontal cells develop their signals with more synapse and more cellular integration than do the receptors.

The RIM fusion consists of five basic layers depicted in Fig. 2. The earliest layer represents an array of high resolution cone photoreceptors (output (1) in Fig. 2). The second layer is a high-scale spatial feature extractor. The function of this layer is represented by the following operator (output (3) in Fig. 2):

$$h_1(\vec{r}) = \frac{\Delta_1^2}{2\pi}\exp\{-|\vec{r}\Delta_1|^2\} - \frac{\Delta_2^2}{2\pi}\exp\{-|\vec{r}\Delta_2|^2\}, \tag{7}$$

where $r = \sqrt{x^2+y^2}$ is the two-dimensional spatial position, Δ_1 is the pixel size of high-resolution image (MRI) and Δ_2 is the pixel size of low-resolution image (PET).

The third layer is the array of low resolution receptors (horizontal cells). This layer's function is modeled by (output (2) and output (4) in Fig. 2):

$$h_2(\vec{r}) = \frac{\Delta_2^2}{2\pi}\exp\{-|\vec{r}\Delta_2|^2\} \tag{8}$$

The fourth and the fifth layers are made of bipolar and ganglion cells. The function of these layers and final retina-inspired fusion model can be illustrated by (output (5) in Fig. 2):

$$f(x,y) = h_1(x,y)\otimes f_1(x,y) + h_2(x,y)\otimes f_2(x,y) \tag{9}$$

where $f_1(x,y)$ and $f_2(x,y)$ are the high and low-resolution images, $h_1(x,y)$ and $h_2(x,y)$ are the filters that introduced in Eqs. (7) and (8). This allows the generation of spatially enhanced multi-spectral images $f(x,y)$, by adding the high resolution spatial features to $f_2(x,y)$ [10] This method does not require the resampling of the images, which is an advantage over the other methods, and can function in any aspect ratio between the MRI and the PET images' pixels. Fig. 3 shows the PET and MRI original images and the results of different parts of the RIM.

3. IHS fusion technique

The IHS transform converts a multispectral image with red, green and blue channels (RGB) to intensity, hue and saturation independent components. The intensity displays the brightness in a spectrum, the hue is the property of the spectral wavelength, and the saturation is the purity of the spectrum. This transform may be used for the fusion of multi-sensor images [7].

The fundamentals of IHS fusion are: (1) aligning the input multispectral image to the high-resolution image; (2) transforming the input multispectral image from RGB to IHS color space; (3) substituting the intensity component with the high-resolution image; and (4) transforming the new substituted IHS components into RGB color space [7,16] This process leads to a fused and enhanced spectral image.

The diagram of this procedure is shown in Fig. 4. A general IHS based is explained by the following equations [7]:

$$\begin{pmatrix} I \\ v1 \\ v2 \end{pmatrix} = \begin{bmatrix} \frac{1}{\sqrt{3}} & \frac{1}{\sqrt{3}} & \frac{1}{\sqrt{3}} \\ \frac{1}{\sqrt{6}} & \frac{1}{\sqrt{6}} & \frac{-2}{\sqrt{6}} \\ \frac{1}{\sqrt{2}} & \frac{-1}{\sqrt{2}} & 0 \end{bmatrix} \begin{pmatrix} R \\ G \\ B \end{pmatrix}, \tag{10}$$

$$H = \tan^{-1}\left(\frac{v1}{v2}\right), \tag{11}$$

$$S = \sqrt{v1^2 + v2^2}. \tag{12}$$

where $v1$ and $v2$ are the transitional values in the above equations. The inverse transform is:

$$\begin{pmatrix} R \\ G \\ B \end{pmatrix} = \begin{bmatrix} \frac{1}{\sqrt{3}} & \frac{1}{\sqrt{6}} & \frac{1}{\sqrt{2}} \\ \frac{1}{\sqrt{3}} & \frac{1}{\sqrt{6}} & \frac{-1}{\sqrt{2}} \\ \frac{1}{\sqrt{3}} & \frac{-2}{\sqrt{6}} & 0 \end{bmatrix} \begin{pmatrix} I \\ S\sin(H) \\ S\cos(H) \end{pmatrix} \tag{13}$$

Triangular spectral model is another type of commonly used IHS transform, where can be depicted as:

$$I = \frac{R+G+B}{3} \tag{14}$$

$$\begin{cases} H = \frac{G-B}{3I-3B}, & S = \frac{I-B}{I}, \quad \text{if } B < R, G \\ H = \frac{B-R}{3I-3R} + 1, & S = \frac{I-R}{I}, \quad \text{if } R < B, G \\ H = \frac{R-G}{3I-3G} + 2, & S = \frac{I-G}{I}, \quad \text{if } G < R, B \end{cases} \tag{15}$$

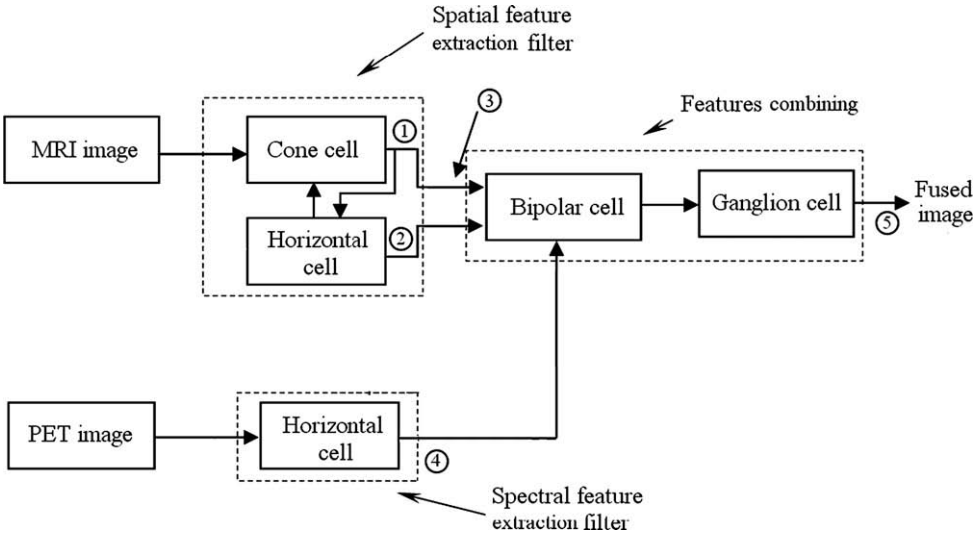

Fig. 2. The structure of image fusion based on RIM.

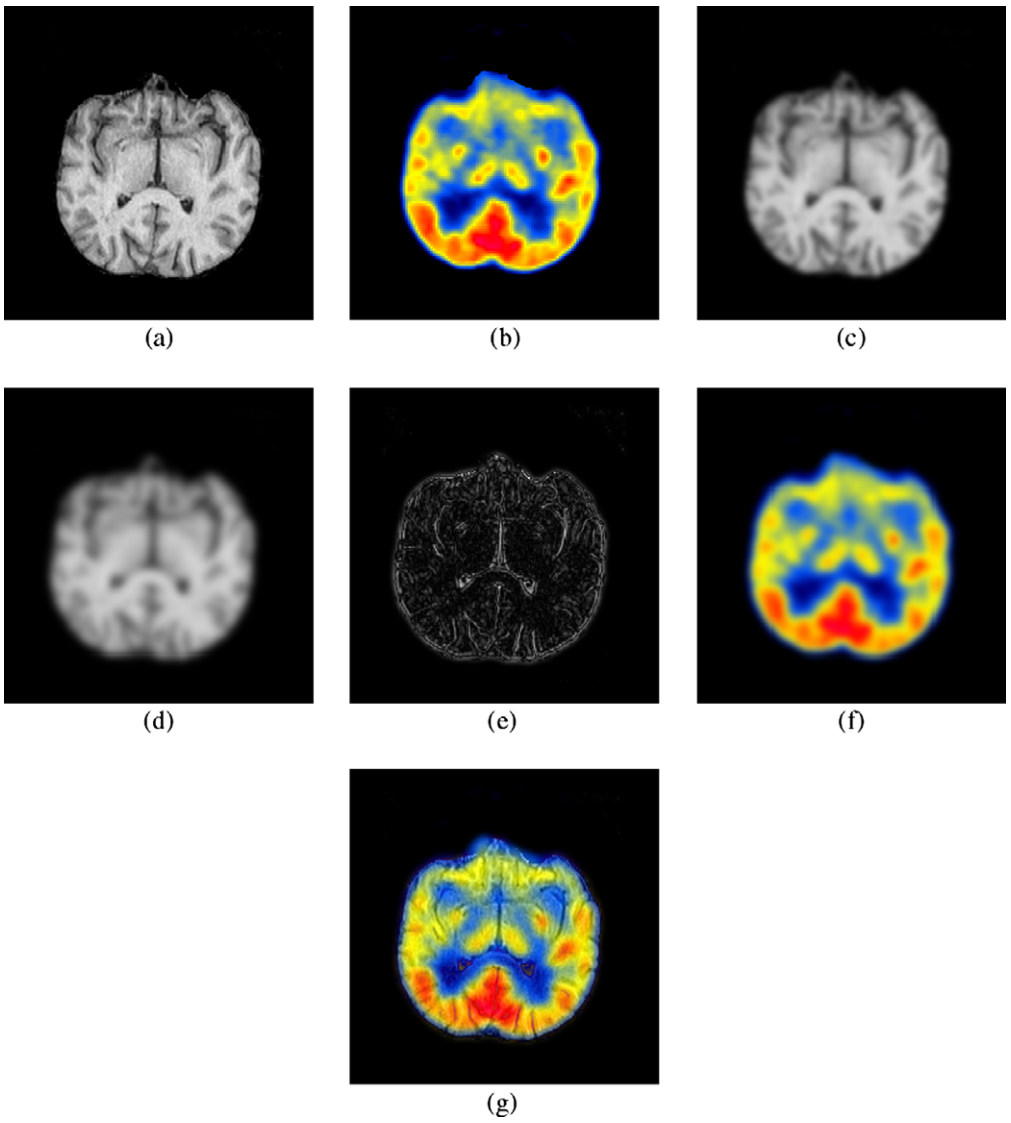

Fig. 3. PET and MRI original images (a and b) and description of the different parts outputs of the retina model in Fig. 2; cone cell output 1 (c), horizontal cell output 2 (d), spatial feature extraction filter output 3 (e), spectral feature extraction filter output 4 (f), and fused image output 5 (g).

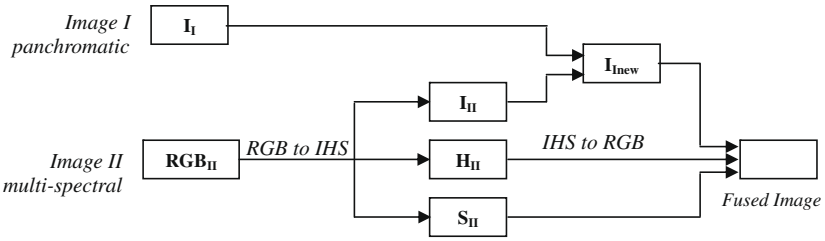

Fig. 4. Diagram of IHS-based fusion.

The inverse IHS transform is shown below:

$$\begin{cases} R = I(1+2S-3SH), \quad G = I(1-S+3SH), \quad B = I(1-S), \\ \qquad\qquad \text{if } B < R, G \\ R = I(1-S), \quad G = I(1+5S-3SH), \quad B = I(1-4S+3SH), \\ \qquad\qquad \text{if } R < G, B \\ R = I(1-7S+3SH), \quad G = I(1-S), \quad B = I(1+8S-3SH), \\ \qquad\qquad \text{if } G < R, B \end{cases} \tag{16}$$

These two IHS fusion models are used to evaluate the proposed model. Furthermore, the IHS triangular model participates in the proposed integrated model.

4. The proposed model

The IHS fusion technique produces high spatial intensity images. However, due to the low correlation between the PET intensity image and the fused images, the spectral distortion is

Table 1
The spectral discrepancies between the fused images and the PET image.

Fusion methods	Dataset 1 mean $D_{k=R,G,B}$	Dataset 2 mean $D_{k=R,G,B}$	Dataset 3 mean $D_{k=R,G,B}$
IHS cylinder model	13.1331	12.9207	14.2609
IHS triangular model	10.3923	10.0261	12.4482
Brovey	10.8129	10.3603	18.3748
DWT	9.4564	10.1253	9.0242
à-trous wavelet	9.4231	10.3461	8.7974
Retina-inspired	8.4595	9.4210	8.0786
Proposed method	**7.7061**	**7.9031**	**6.0118**

considerable (Table 1). The retina-inspired image fusion can preserve more spectral information than other conventional fusion methods (Table 1). However, the spatial details in the retina-inspired-fusion results are often different from the MRI image, which introduces spatial distortion into the results. To improve the IHS and the retina-inspired fusion techniques, and to overcome the deficiencies of the two methods, an integrated fusion method is proposed in this paper. To attain a smooth combination of spectral and spatial features, the proposed method employs the IHS triangular model to integrate the PET spectral (color) information with the MRI spatial detail information which is depicted in Fig. 5. This fusion process generates a new high resolution color image. The new image contains both the spatial detail of the MRI source image, and the color detail of the PET source image, simultaneously.

According to Fig. 5, in the first stage, the PET image is transformed into the IHS-triangular-model components. The PET image should be aligned to the MRI image in advance. In the second stage, histogram matching is applied to match the histogram of the MRI image with the PET-intensity component. The third stage is performed by combining the new MRI (called New Pan) and original PET-intensity component, using retina-inspired fusion method. In this stage a new intensity image is obtained, which contains the same spatial detail of the original MRI and has the same intensity distribution to the original PET. Ultimately, this process is completed by inverse HIS transform of the new intensity and the old hue and saturation components back into RGB space.

5. Experimental results and discussions

The test data consist of color PET images and high resolution MRI images. The spatial resolution of MRI images and PET images are 256×256 and 128×128 pixels. The color PET images were registered to the corresponding MRI images. All images have been downloaded from the Harvard university site (http://www.med.harvard.edu/AANLIB/home.html). The brain images are classified into three groups (normal axial, normal coronal and Alzeimer's disease dataset images). The IHS transform, the retina-inspired fusion transform, Brovey, DWT, à-trous wavelet and the proposed method were employed to fuse the image datasets. The original images and fusion results are displayed in Figs. 6–8.

It can be observed that the IHS-based fusion transforms have fairly good spectrum and better spatial feature integration

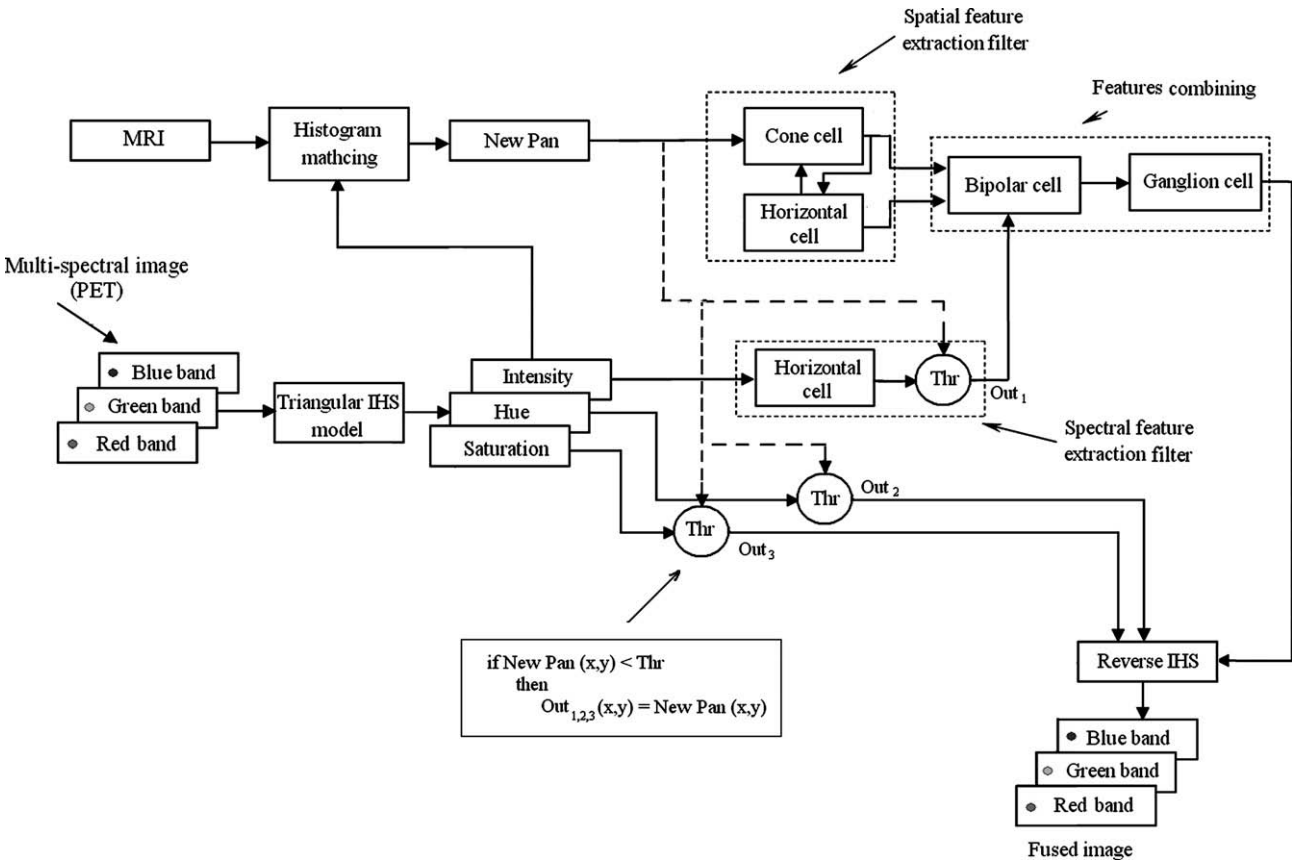

Fig. 5. Diagram of the proposed IHS and retina-inspired fusion integrated method.

(Figs. 6–9). Nevertheless, the spectral distortions are the greatest problem faced here and much spectral information is lost in IHS fusion method. Visual analysis demonstrates that the retina-inspired fused results have low spatial resolutions; however, their spectral intensities are strong. The enlarged version of the various fused images and arrows in Fig. 9 show that more spatial information is preserved in the proposed fusion method. Apparently, the results from the proposed method (notice the arrows in Figs. 6–8i or Fig. 9) appear the best among all the results visually.

In the proposed method, the color information was least distorted, the spatial details are as clear as the original MRI, and the integration of spectral and spatial features is natural. The structures such as the vermis of the cerebellum (encircled in Fig. 9-7b are clearly visible in the MRI and Fig. 9-7i but they loose much of their anatomical contour in other fusion methods. The fibrous also strands of light matter in the cerebellar lobes (Fig. 9) are nicely distinguishable in the proposed method.

The importance of the statistical assessment of the quality of different fusion techniques has increased because of the widespread use of multi-sensor and multi-spectral images in medical diagnoses. Therefore, superior quality evaluation tools are required to compare the results achieved by different fusion techniques [23]. The perfect fused-image is often unknown and very difficult to create. This problem leads to the inadequacy of the fused images in being compared with a gold standard. For human observation, the performance of fusion algorithms can be measured in terms of enhancement in user performance in tasks like recognition, detection, or classification. This process requires a clear task for which quantitative measurements can be carried out to describe human performance. However, this requires more time and often more costly experiments with human subjects.

Several computational image fusion quality assessment metrics have been proposed in recent years [23,24]. Metrics that precisely relate to human observer performance are of great value but are very difficult to implement, and thus are not available yet. In order to compare different image fusion algorithms objectively, we also need largely available multi-spectral or multi-sensor datasets that can be used to evaluate the existing and new algorithms.

The proposed method is compared with the conventional retina-inspired-based, IHS cylinder model, IHS triangular model, Brovey, DWT, and à-trous wavelet transform methods. A suitable fusion method should preserve the spectral characteristics of the source multispectral image and the high spatial resolution characteristics of the source high-resolution image. In this paper, two evaluation criteria are used for quantitative assessment of the fusion performance.

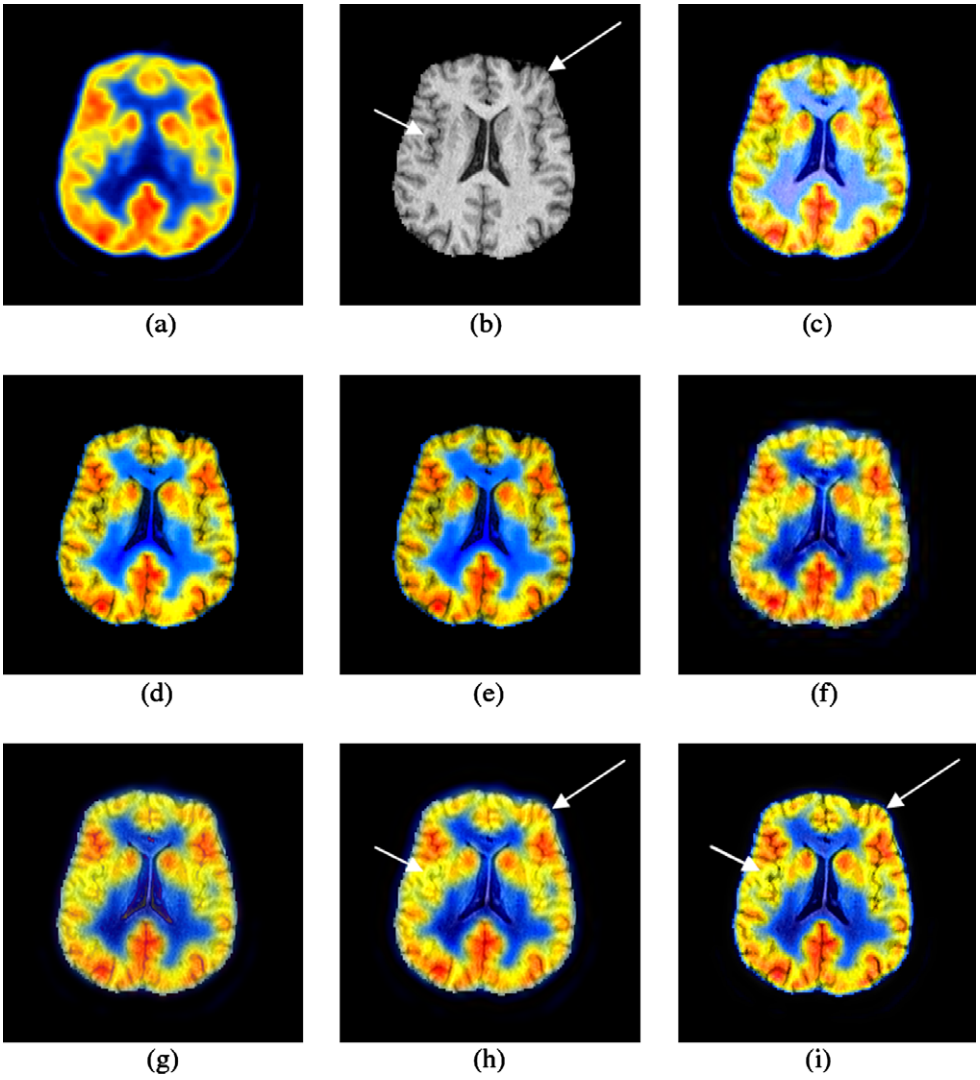

Fig. 6. Normal axial PET and MRI images (a and b), IHS cylinder model (c), IHS triangular model (d), Brovey (e), DWT (f), à-trous wavelet (g), retina-inspired based (h), and proposed method (i).

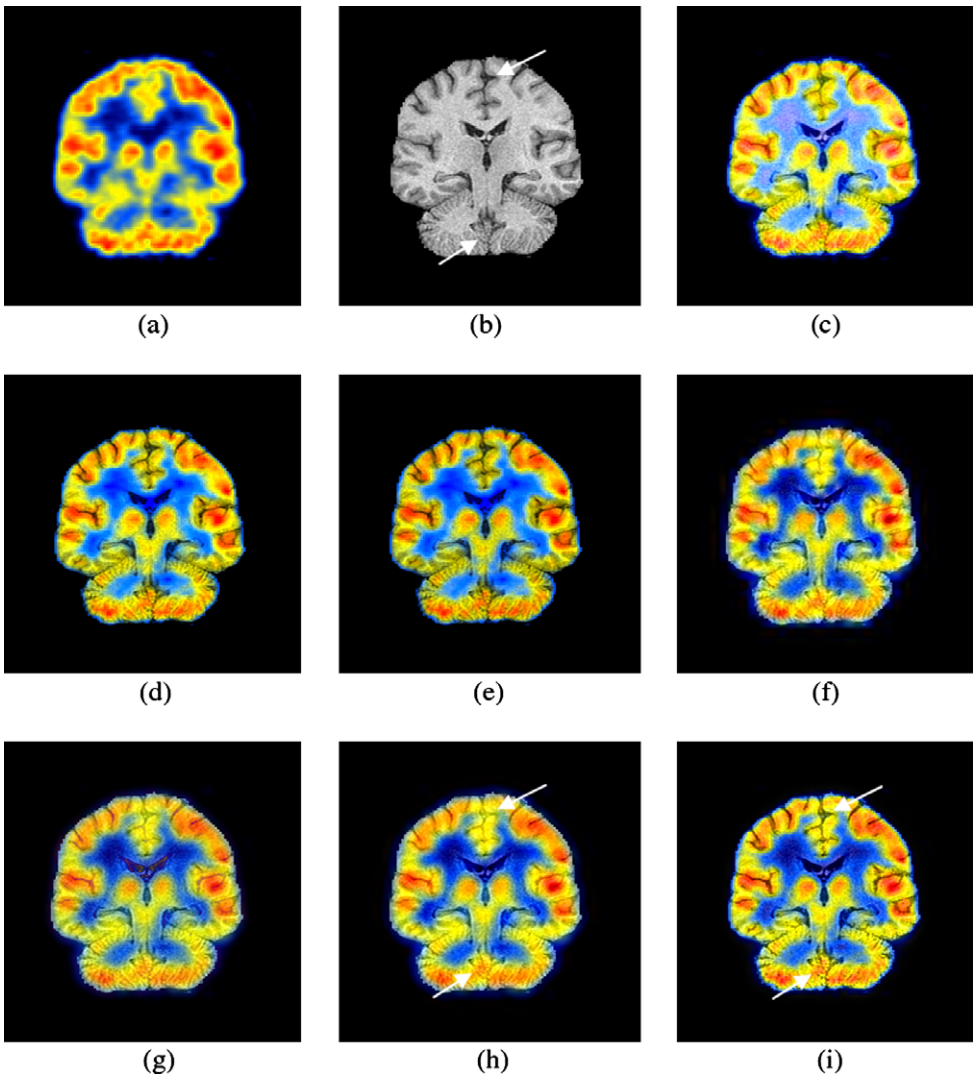

Fig. 7. Normal coronal PET and MRI images (a and b), IHS cylinder model (c), IHS triangular model (d), Brovey (e), DWT (f), à-trous wavelet (g), retina-inspired based (h) and proposed method (i).

5.1. Discrepancy and average gradient

The discrepancy measures the spectral quality of a fused image at each band by D_k [25]

$$D_k = \frac{1}{P.Q}\sum_{x=1}^{P}\sum_{y=1}^{Q}|f_k(x,y) - f_{2k}(x,y)| \quad k = R,G,B \tag{17}$$

where $f_k(x,y)$ and $f_{2k}(x,y)$ are the pixel values of the fused and original images at position (x,y); in this paper $P = 256$, and $Q = 256$. A tiny discrepancy means an acceptable fusion result. For the spatial quality, we use the average gradient to calculate the performance of the fused image [25]:

$$Avg_k = \frac{1}{(P-1)\cdot(Q-1)}\sum_{x=1}^{P-1}\sum_{y=1}^{Q-1}\sqrt{\frac{\left(\frac{\partial f_k(x,y)}{\partial x}\right)^2 + \left(\frac{\partial f_k(x,y)}{\partial y}\right)^2}{2}}$$
$$k = R,G,B \tag{18}$$

The average gradient reflects the clarity of the fused image. It can be used to measure the spatial resolution of the fused image, i.e., a larger average gradient shows a higher spatial resolution.The overall image fusion performance measure can be described as:

$$\text{O.P} = \frac{\sum_k |D_k - Avg_k|}{3}, \quad k = R,G,B \tag{19}$$

The small amount of overall performance (O.P) means a higher overall fusion quality.

Table 1 shows the spectral discrepancies between the images obtained by different fusion algorithms and the source multispectral image. The average gradients of the images obtained by different fusion algorithms are shown in Table 2. From these two tables, we can conclude that the proposed algorithm can preserve high spatial resolution characteristics of the source high-resolution image. In addition, the spectral distortion introduced to the proposed fusion method is less than the other algorithms. Table 3 represents overall performance of different fusion methods. These results demonstrate that the proposed method preserves more spatial features with less spectral distortion.

5.2. Mutual information:

Mutual information (MI) is a fundamental concept of the information theory to compute the statistical dependence between two random variables [26] MI has been applied in many areas including, information fusion, and image registration. Given two random

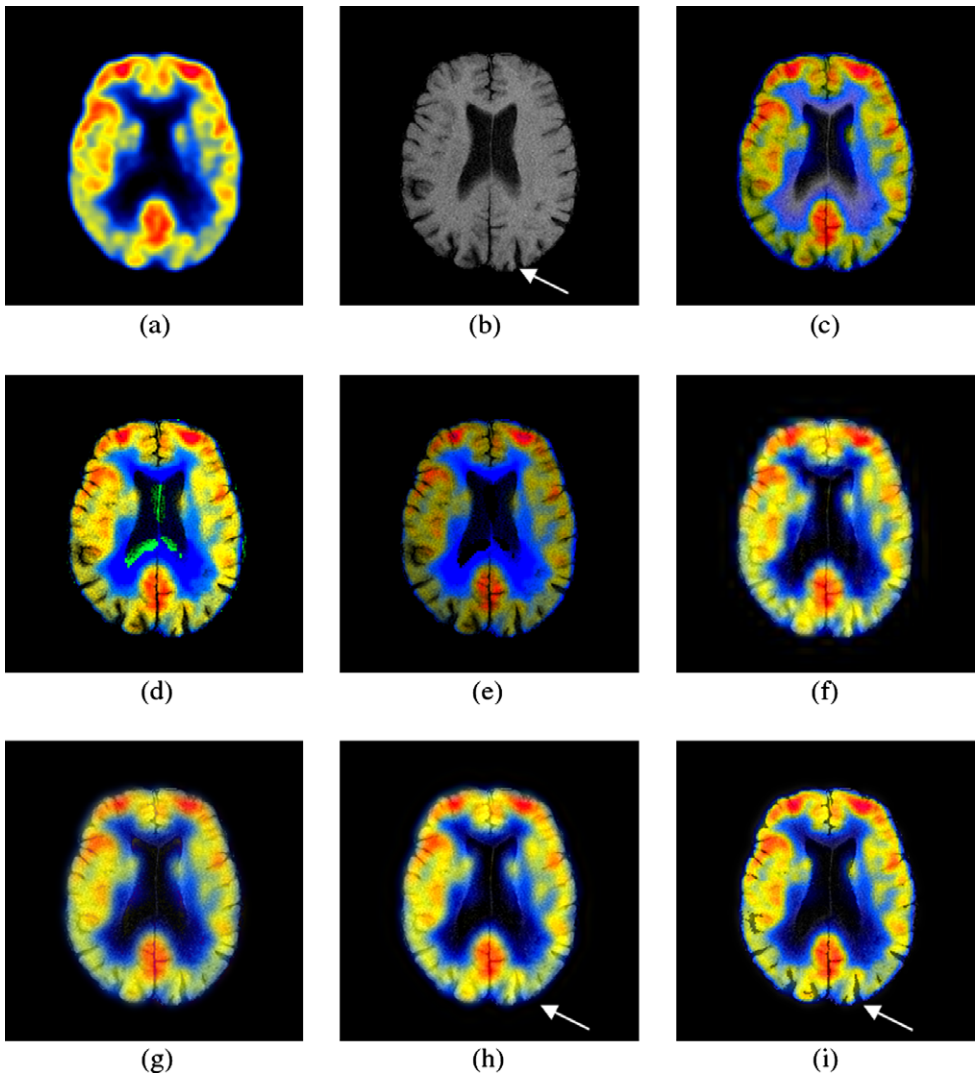

Fig. 8. Alzheimer's disease PET and MRI images (a and b), IHS cylinder model (c), IHS triangular model (d), Brovey (e), DWT (f), à-trous wavelet (g), retina-inspired based (h) and proposed method (i).

variables, A and B, with marginal probability distributions, $p_A(a)$ and $p_B(b)$, nd joint probability distribution p_{AB} (a, b), MI is

$$\mathrm{MI}(A,B) = \sum_{a,b} p_{AB}(a,b) \log \frac{p_{AB}(a,b)}{p_A(a)p_B(b)}, \tag{20}$$

MI is related to entropy by the following equations:

$$\begin{aligned} \mathrm{MI}(A,B) &= H(A) + H(B) - H(A,B) \\ &= H(A) - H(A \setminus B) \\ &= H(B) - H(B \setminus A) \end{aligned} \tag{21}$$

where $H(A)$ and $H(B)$ are the entropy of A and B and $H(A, B)$ is their joint entropy. $H(A \setminus B)$ and $H(B \setminus A)$ are the conditional entropies of A given B and of B given A, respectively. Using Shannon's definition of entropy, these entropies can be shown as:

$$H(A) = -\sum_{a} p_A(a) \log p_A(a), \tag{22}$$

$$H(A,B) = -\sum_{a,b} p_{AB}(a,b) \log p_{AB}(a,b) \tag{23}$$

$$H(A \setminus B) = -\sum_{a,b} p_{AB}(a,b) \log p_{A\setminus B}(a \setminus b) \tag{24}$$

MI can determine the statistical dependence or information redundancy between two random variables. If we represent the original multispectral image and the fused image as random variables, MI can be used to estimate the dependency between them. It is useful to know how much information the fused image provides the PET image.

Two input images A (PET), B (MRI) and a new fused image F are considered, the amount of information that F contains about A and B can be calculated as:

$$I_{FA}(f,a) = (1/3). \sum_{k} \sum_{f,a} p_{FA}(f_k,a_k) \log \frac{p_{FA}(f_k,a_k)}{p_F(f_k) \cdot p_A(a_k)}, \quad k = R,G,B \tag{25}$$

$$I_{FB}(f,b) = (1/3) \cdot \sum_{k} \sum_{f,b} p_{FB}(f_k,b) \log \frac{p_{FB}(f_k,b)}{p_F(f_k) \cdot p_B(b)}, \quad k = R,G,B \tag{26}$$

The image fusion performance measure can be defined by [27]:

$$M_F^{AB} = \frac{I_{FA}(f,a) + I_{FB}(f,b)}{2} \tag{27}$$

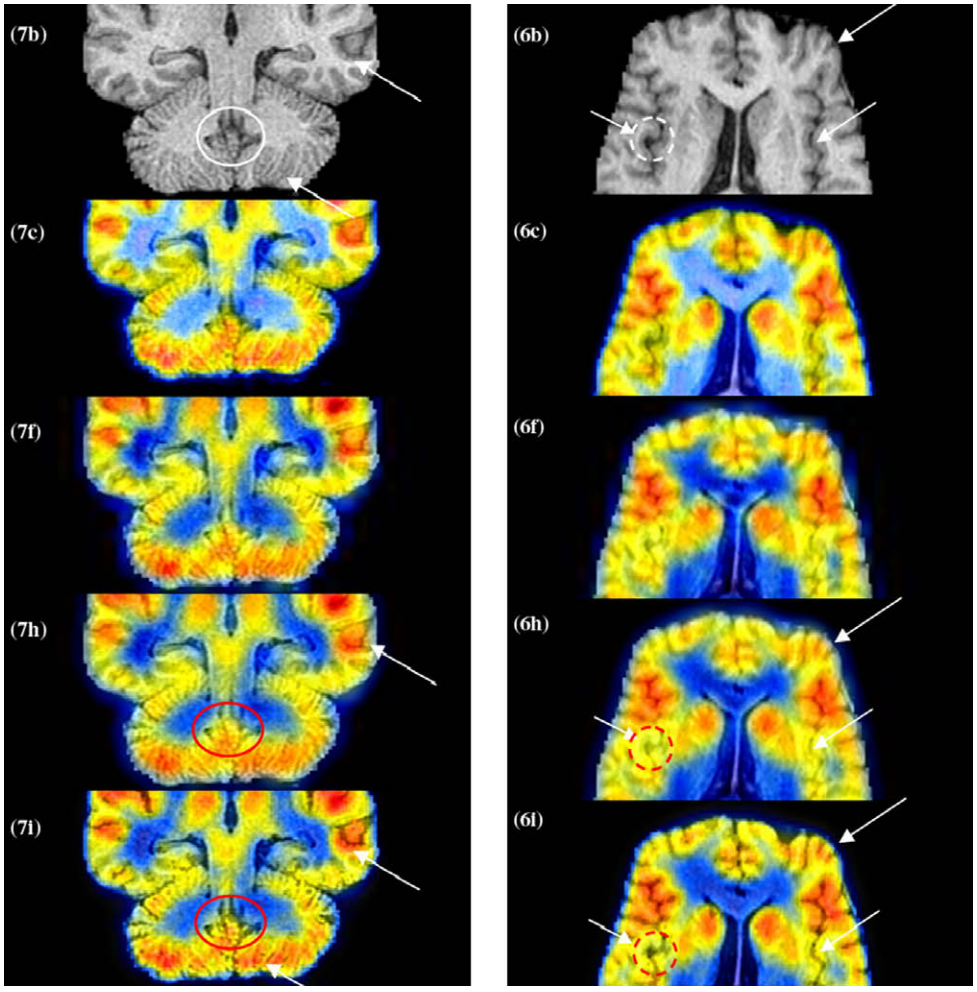

Fig. 9. Enlarging various fused images (Figs. 6 and 7) to see better the differences in MRI spatial correlation. The arrows in the images show that the proposed algorithm (6i and 7i) preserves the more spatial information content.

Table 2
The average gradients of the fused images.

Fusion methods	Dataset 1 mean $Avg_{k=R,G,B}$	Dataset 2 mean $Avg_{k=R,G,B}$	Dataset 3 mean $Avg_{k=R,G,B}$
IHS cylinder model	4.7886	5.6167	4.3891
IHS triangular model	4.4681	5.3782	4.9562
Brovey	4.4945	5.3246	3.4983
DWT	4.6829	5.4641	4.2383
à-trous wavelet	4.2494	5.0211	3.8208
Retina-inspired	4.4326	5.2019	4.0024
Proposed method	**5.3603**	**6.2927**	**5.0353**

Table 3
The overall fusion performance measure based on discrepancy and average gradient.

Fusion methods	Dataset 1 O.P	Dataset 2 O.P	Dataset 3 O.P
IHS cylinder model	8.3445	7.3040	9.8718
IHS triangular model	5.9242	4.6479	7.4920
Brovey	6.3184	5.0356	14.8765
DWT	4.7735	4.6612	4.7859
à-trous wavelet	5.1737	5.3250	4.9766
Retina-inspired	4.0269	4.2192	4.0762
Proposed method	**2.3457**	**1.6104**	**0.9765**

Table 4
The fusion methods performance measure based on entropy and mutual information.

Fusion methods	M_F^{AB} (Dataset 1)	M_F^{AB} (Dataset 2)	M_F^{AB} (Dataset 3)
IHS cylinder model	0.6414	0.6487	0.5722
IHS triangular model	0.6434	0.6566	0.5770
Brovey	0.6446	0.6476	0.5808
DWT	0.5836	0.5886	0.5323
à-trous wavelet	0.6106	0.6093	0.5626
Retina-inspired	0.6517	0.6489	0.6105
Proposed method	**0.6541**	**0.6551**	**0.6230**

Table 4 shows that the amount of information of the fused image, achieved by the proposed method, is the highest. These statistical assessment findings agree with those of the visual analysis, the proposed method has the least color distortions and contains more spatial information.

6. Conclusions

In this paper, we proposed a new method for PET and MRI images fusion. We assume PET images are shown in pseudo-color, and therefore, treat them as color images. The PET produces images with suitable color and low spatial resolutions, while MRI provides appropriate spatial resolution with no color information content. The

algorithms and fusion results of the most popular IHS fusion and the RIM fusion technique are reviewed to find the weak points of both fusion techniques and use their potencies. The RIM image fusion usually can preserve more color information than the IHS method but it preserves less spatial information content. The presented algorithm integrates the advantages of both IHS and RIM fusion methods to improve the color and spatial information content.

The proposed fusion results were compared with those of the IHS (the cylinder and the triangular model), Brovey, DWT, and à-trous wavelet and conventional retina-inspired-based fusion methods. Visual analyses show that the results from the proposed method appear best among all the results. In the proposed fused images the color information was least distorted, the spatial details were as clear as the original MRI, and the integration of color and spatial features was normal. The statistical analyses tools such as entropy, mutual information, discrepancy, and average gradient are demonstrated that the proposed algorithm did considerably increase spatial information content and reduce the color distortion compared to the counterpart fusion methods. Those statistical assessment findings agree with the visual analysis. An advantage of this method, similar to retina-inspired fusion method, is that it can perform in any aspect ratio between images' pixels and does not require resampling process.

Acknowledgement

The authors would like to sincerely thank the anonymous reviewers for their useful comments which helped us to improve the paper.

References

[1] A.L. Grosu, W.A. Weber, M. Franza, Reirradiation of recurrent high-grade gliomas using amino acid PET (SPECT)/CT/MRI image fusion to determine gross tumor volume for stereotactic fractionated radiotherapy, International Journal of Radiation Oncology Biology Physics 63 (2) (2005) 511–519.
[2] M. Jan, K. Chuang, G. Chen, A three-dimensional registration method for automated fusion of micro PET-CT-SPECT whole-body images, IEEE Transactions on Medical Imaging 24 (7) (2005) 886–993.
[3] A. Polo, F. Cattani, A. Vavassori, MR and CT image fusion for postimplant analysis in permanent prostate seed implants, International Journal of Radiation Oncology Biology Physics 60 (5) (2004) 1572–1579.
[4] P. Calvini, A.M. Massone, F.M. Nobili, G. Rodriguez, Fusion of the MR image to SPECT with possible correction for partial volume effects, IEEE Transactions on Nuclear Science 53 (1) (2006) 189–197.
[5] D. Rajasekar, N.R. Datta, R.K. Gupta, Multimodality image fusion in dose escalation studies of brain tumors, Journal of Applied Clinical Medical Physics 4 (1) (2003) 8–16.
[6] A. Goshtasby, S. Nikolov, Image fusion: advances in the state of the art, Information Fusion 8 (2) (2007) 114–118.
[7] T.M. Tu, S.C. Su, H.C. Shyu, P.S. Huang, A new look at IHS-like image fusion methods, Information Fusion 2 (3) (2001) 177–186.
[8] M. González-Audícana, J.L. Saleta, R.G. Catalán, R. García, Fusion of multispectral and panchromatic images using improved IHS and PCA mergers based on wavelet decomposition, IEEE Transaction on Geoscience and Remote Sensing 42 (6) (2004) 1291–1299.
[9] C. Pohl, J.L. Van Genderen, Multisensor image fusion in remote sensing: concepts methods and applications, International Journal of Remote Sensing 19 (5) (1998) 823–854.
[10] H. Ghassemian, A retina based multi-resolution image fusion, in: Proceedings of IEEE International Geoscience and Remote Sensing Symposium, IGRSS2001, July 2001.
[11] W. Shi, Ch. Zhu, C. Zhu, X. Yang, Multi-band wavelet for fusing SPOT panchromatic and multispectral images, International Journal of Photogrammetric Engineering and Remote Sensing 69 (5) (2003) 513–520.
[12] A. Wang, S. Haijing, G. Yueyang, The application of wavelet transform to multi-modality medical image fusion, in: Proceedings of IEEE International Conference on Networking, Sensing and Control, April 2006, pp. 270–274.
[13] H. Zhang, L. Liu, N. Lin, A novel wavelet medical image fusion method, in: International Conference on Multimedia and Ubiquitous Engineering, April 2007, pp. 548–553.
[14] H. Ghassemian, Multisensor image fusion by multiscale filter banks, in: Proceeding of IEEE International Conference on Image Processing ICIP2001, October 2001.
[15] Y. Zheng, E.A. Essock, B.C. Hansen, A.M. Haun, A new metric based on extended spatial frequency and its application to DWT based fusion algorithms, Information Fusion 8 (2) (2007) 177–192.
[16] Y. Zhang, G. Hong, An IHS and wavelet integrated approach to improve pan-sharpening visual quality of natural colour IKONOS and QuickBird images, International Journal of Information Fusion 6 (3) (2005) 225–234.
[17] T.M. Tu, W.C. Cheng, C.P. Chang, P.S. Huang, J.C. Chang, Best tradeoff for high-resolution image fusion to preserve spatial details and minimize color distortion, IEEE Geoscience and Remote Sensing Letters 4 (2) (2007) 302–306.
[18] H. Kolb, The neural organization of the human retina, in: J.R. Heckenlively, G.B. Arden (Eds.), Principles and Practices of Clinical Electrophysiology of Vision, Mosby Year Book Inc., St. Louis, 1991, pp. 25–52.
[19] H. Kolb, How the retina works, Journal of American Scientist 91 (2003) 23–35.
[20] S. Shah, M.D. Levine, Visual information processing in primate cone pathways. I. A model, IEEE Transactions on Systems, Man and Cybernetics, Part B 26 (2) (1996) 259–274.
[21] C.A. Morillas, S.F. Romero, A. Martínez, F.J. Pelayo, E. Ros, E. Fernández, A design framework to model retinas, BioSystems 87 (2–3) (2007) 156–163.
[22] J. Partzsch, C. Mayr, R. Schuffny, Building Gabor filters from retinal responses, Transactions on Engineering, Computing and Technology 19 (2007) 211–216.
[23] Z. Wang, D. Ziou, C. Armenakis, D. Li, Q. Li, A comparative analysis of image fusion methods, IEEE Transactions Geoscience and Remote Sensing 43 (6) (2005) 1392–1402.
[24] W. Shi, Ch. Zhu, Y. Tian, J. Nichol, Wavelet-based image fusion and quality assessment, International Journal of Applied Earth Observation and Geoinformation 6 (2005) 241–251.
[25] Z. Li, Zh. Jing, X. Yang, Color transfer based remote sensing image fusion using non-separable wavelet frame transform, Pattern Recognition Letters 26 (2005) 2006–2014.
[26] G. Piella, A general framework for multiresolution image fusion: from pixels to regions, Information Fusion 4 (4) (2003) 259–280.
[27] Y. Chen, R.S. Blum, Experimental tests of image fusion for night vision, in: International Conference on Information Fusion (7th), 2005, pp. 491–498.